Article

Wetland Mapping Using SAR Data from Sentinel-1A and TanDEM-X Missions: Comparative Study in the Biebrza Floodplain (Poland)

Magdalena Mleczko * and Marek Mróz

Institute of Geodesy, University of Warmia and Mazury in Olsztyn, ul. Oczapowskiego 1, 10-719 Olsztyn, Poland;
* Correspondence: magdalena.mleczko@uwm.edu.pl; Tel.: +48-89-523-3549

Abstract: This research is related to the eco-hydrological problems of herbaceous wetland drying and biodiversity loss in the floodplain lakes of the Middle Basin of the Biebrza river (Poland). An experiment was set up, whose main goals were: (i) mapping the vegetation types and the temporarily or permanently flooded areas, and (ii) comparing the usefulness of C-band Sentinel-1A (S1A) and X-band TerraSAR-X/TanDEM-X (TSX/TDX) for mapping purposes. The S1A imagery was acquired on a regular basis using the dual polarization VV/VH and the Interferometric Wide Swath Mode. The TSX/TDX data were acquired in quad-pol, a fully polarimetric mode, during the Science Phase. The paper addresses the following aspects: i) wetland mapping with S1A multi-temporal series; ii) wetland mapping with fully polarimetric TSX/TDX data; iii) comparing the wetland mapping using dual polarization TSX/TDX subsets, i.e. HH-HV, HH-VV and VV-VH; iv) comparing wetland mapping using S1A and TSX/TDX data based on the same polarization (VV-VH); v) studying the suitability of the Shannon Entropy for wetland mapping; and vi) assessing the contribution of interferometric coherence for wetland classification. The experimental results show main limitations of the S1A dataset, while they highlight the good accuracy that can be achieved using the TSX/TDX data, especially those taken in fully polarimetric mode.

Keywords: Sentinel-1A; TanDEM-X science phase; wetlands mapping

1. Introduction

As stated in [1], the need for wetland mapping has never been greater as the world's population continues to increase. Climate change impact combined with human activity transforming wetlands into meadows or pastures have led, in many geographical contexts, to wetlands degradation, drying of soils and biodiversity loss. Nowadays, positive water balance and longer period of water stagnation are crucial factors in wetlands re-naturalization process and conservation.

The main motivation of this research is related to the eco-hydrological problems of herbaceous wetland drying and biodiversity loss in the floodplain lakes of the Middle Basin of the Biebrza river (Poland). In this area, the problems of soil moisture and biomass estimation have been intensively studied in the past [2,3]. The main hydrological concern in this area is how to retain for longer periods the water from early spring flooding. The deficit of water is a factor influencing the life conditions of ichthyofauna and avifauna. Further consequences of water deficit are the unfavourable vegetation succession and the reduction of the quantity of species.

Eco-hydrological investigations of wetlands bring essential information for ecological inventory and wetland management. They need to be based on detailed mapping of the vegetation and the monitoring of changing water conditions. Wetland mapping using radar remote sensing has developed rapidly over the past years thanks to the wide availability of SAR imagery and the increased geometric resolution of SAR sensors. Wetlands have specific and advantageous features in relation to the microwave scattering mechanism. In fact, microwaves are sensitive to

Peer-reviewed version available at Remote Sens. 2018, 10, 78; doi:10.3390/rs10010078

differences in water content and surface roughness. An increase of moisture or roughness results in an increase of the backscatter. In addition, the presence of water sheet with partially submerged plant communities creates the conditions for phase coherence preservation due to the double bounce effect. This can be one of the discriminator for land cover mapping [4,5]. In general, the results of SAR-based land cover and vegetation mapping depend on the used wavelength (X-, C- or L- band) and data polarization (vertical, VV, horizontal, HH, or orthogonal, VH or HV). This is one of the issues treated in this work.

The launch of the ESA's Sentinel-1A (S1A) satellite, in 2014, opened a new era of SAR mapping. Free and open access is guaranteed to C-band SAR scenes in the dual polarization configuration VV-VH. Key advantages of S1A include the observation of large swaths (250 km), the 12-day repetition cycle (using S1A or S1B only), the availability of two operational sensors and the free of charge SAR imagery. Compared with TerraSAR-X and TanDEM-X (TSX/TDX) data, S1A offers a reduced geometric resolution and a fixed polarimetric configuration. In this work the potential of S1A for wetland mapping is addressed.

The availability of fully polarimetric SAR (HH/HV/VH/VV channels) could provide additional information on the structure and moisture of the vegetation, thus improving the utility of SAR data for wetland mapping [1,6,7]. However, the sources of fully polarimetric spaceborne SAR data are limited to C-band Radarsat-2 and L-band ALOS-PALSAR. In X-band, interesting experimental campaigns based on the TSX/TDX satellites, forming a "fully polarimetric constellation", were carried out by DLR in 2010 and 2014-2015, for a limited number of test sites in the globe. In addition to the evaluation of the potential of S1A imagery, in this work we decided to investigate the "fully polarimetric TSX/TDX constellation". The Biebrza area was proposed to DLR as a test site during the Science Phase of TSX/TDX mission. The main goals of this test site were: (i) mapping the vegetation types/associations/species and the temporarily or permanently flooded areas, and (ii) comparing the usefulness of S1A and TSX/TDX for mapping purposes. The main outcomes of this research are described in this paper. To summarize, this work addresses the following main aspects:

1. Mapping wetland with C-band S1A alone, based on multi-temporal series of SAR images.
2. Mapping wetland with experimental fully polarimetric quad-pol X-band TSX/TDX data.
3. Compare the wetland mapping using dual polarization TSX/TDX subsets, i.e. HH-HV, HH-VV and VV-VH. These subsets represent the standard products that could be acquired by an operational X-band SAR sensor.
4. Compare wetland mapping using S1A and TSX/TDX data based on the same polarization (VV-VH) and covering the same observation period.
5. Study the suitability of the Shannon Entropy as polarimetric descriptor of wetland land cover, starting from dual-pol and quad-pol data.
6. Assess the contribution of interferometric coherence as an additional layer for land cover classification.

This paper is organized as follows. Section 2 describes the materials and methods. This includes the description of the study area and of the analysed S1A and TSX/TDX datasets; the discussion of the image pre-processing carried out in this study; and the description of the image classification approach. Sections 3 discusses the main results of this work. Finally, Section 4 includes the main conclusions of this study.

2. Materials and Methods

2.1. Description of the study area and the available ground truth

The Area of Interest (AoI) is part of the Middle Basin of the Biebrza Valley, in the Biebrza National Park (BbPN) [8], located in North-Eastern Poland (Figure 1). The Biebrza marshes represent an important wetland area, which is included in United Nations Ramsar Convention on Wetlands [9]. The investigated area is mainly characterized by numerous meanders of the main stream and many oxbow lakes, with the different degree of hydrological connectivity. The study area was

Peer-reviewed version available at *Remote Sens.* **2018**, *10*, 78; doi:10.3390/rs10010078

restricted to natural vegetation communities only, while the agricultural areas were excluded. The most dominating vegetation species are bur-reed, sweet-grass, reed canary, lakeshore bulrush, bulrush, common reed, sedge, dogwood, willow scrub and deciduous forest. The most characteristic phenomenon in this area is the occurrence of an annual, spring flooding, which causes the increase in the biodiversity of the area. The snow melt is the most important source of water, but the period of water stagnation is relatively short due to the artificial drainage network built 50 years ago that enables fast water transfer from the Middle to the Lower Basin.

An important database of the vegetation and land cover of the study area was established using data from external GIS databases, land register and several field surveys made in correspondence to the radar image acquisition dates. The ground truth collection was made by botanists and hydrologists with the support of aerial imagery from several surveys using a UAS system equipped with RGB camera. The photointerpretation of multi-temporal RGB images combined with in situ GPS measurements allowed us to draw the accurate polygons of the different thematic classes of the area.

The Table 1 contains the information on the vegetation types considered in this study, and their statistical representation using S1A and TSX/TDX data.

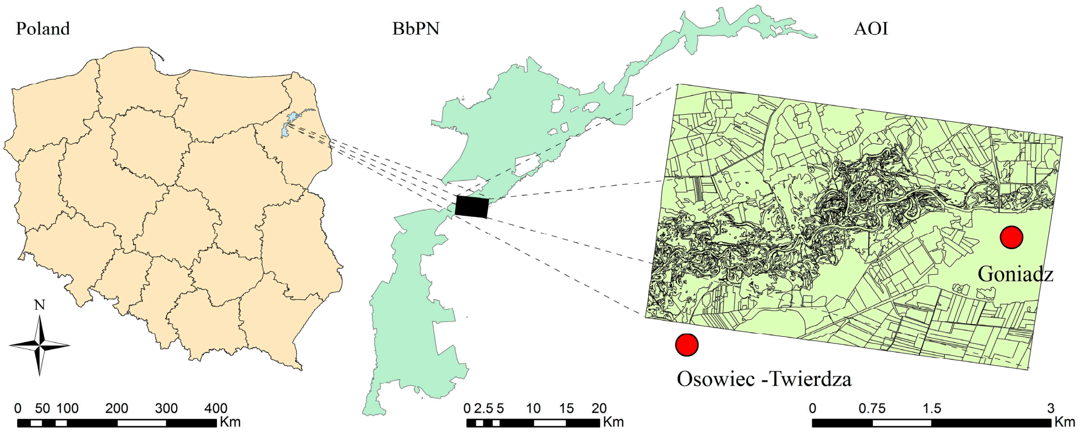

Figure 1. Location of the study area in North-Eastern Poland.

Table 1. List of the vegetation types recognized in the AoI, number of parcels and their area.

No	Class	Number of parcels	Number of pixels TSX/TDM	Number of pixels Sentinel-1A	Area [ha]
1	grasslands/ meadows	15	14968	979	9.36
2	deciduous forest	10	39830	2553	24.89
3	bur-reed	3	371	20	0.23
4	sweet-grass	23	16712	1137	10.45
5	reed canary	19	7848	549	4.91
6	lakeshore bulrush	4	454	34	0.28
7	bulrush	13	850	71	0.53
8	common reed	47	17556	1260	10.97
9	sedge	25	19062	1266	11.91
10	water bodies	14	56510	3775	35.32
11	dogwood	9	933	66	0.58
12	willow scrub	7	2052	138	1.28

Peer-reviewed version available at *Remote Sens.* **2018**, *10*, 78; doi:10.3390/rs10010078

2.2. Sentinel-1A and TSX/TDX datasets

In this study, two radar image time series were used: S1A and TSX/TDX. The S1A imagery was acquired on a regular basis using the dual polarization VV/VH and the Interferometric Wide Swath Mode. The S1A dataset consists of Single Look Complex (SLC) images, acquired with a look angle of 38.9º. The TSX/TDX data were acquired in quad-pol, fully polarimetric mode during the 15-months of the Science Phase. The main goal of the Science Phase was the demonstration of new SAR techniques, see for details [10]. The fully polarimetric coherent data were acquired using a Dual Receive Antenna. The used TSX/TDX images were Co-registered Single look Slant range Complex (CoSSC) products, acquired in StripMap Bistatic mode, with a look angle of 36º. The main characteristics of the TSX/TDX and S1A data are shown in Table 2. The data cover a 2-month period (Figure 2), which includes a spring flooding and the subsequent dynamic vegetation development of the wetlands.

Table 2. TSX/TDX and Sentinel -1A data characteristics.

Mission	TSX/TDX	Sentinel-1A
Bandwidth	9.65 GHz	5.405 GHz
Wavelength	X (3 cm)	C (5.6 cm)
Imaging Mode	Stripmap Bistatic	Interferometric Wide
Track	stripFar_009	153
Orbit	Ascending	Descending
Product	CoSSC	SLC
Ground resolution, rg by az	1.2 by 6.6 m	3.1 by 21.7 m
Pixel spacing, rg by az	0.9 by 2.2 m	2.3 by 13.8 m
Polarization	Quad (HH, HV, VH, VV)	Dual (VV, VH)
Incidence angle	36º	38.9º
Revisit time	11 days	12 days
Covered area	15 by 30 km	250 by 170 km

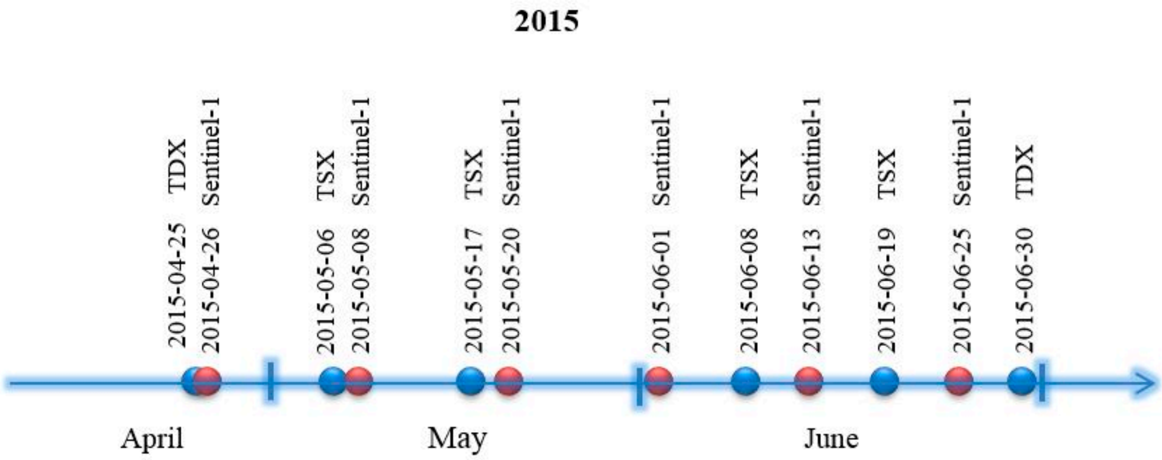

Figure 2. Satellite images used in the study.

2.3. Image pre-processing

This work involved a set of image pre-processing steps. The workflow of such an image pre-processing is shown in Figure 3.

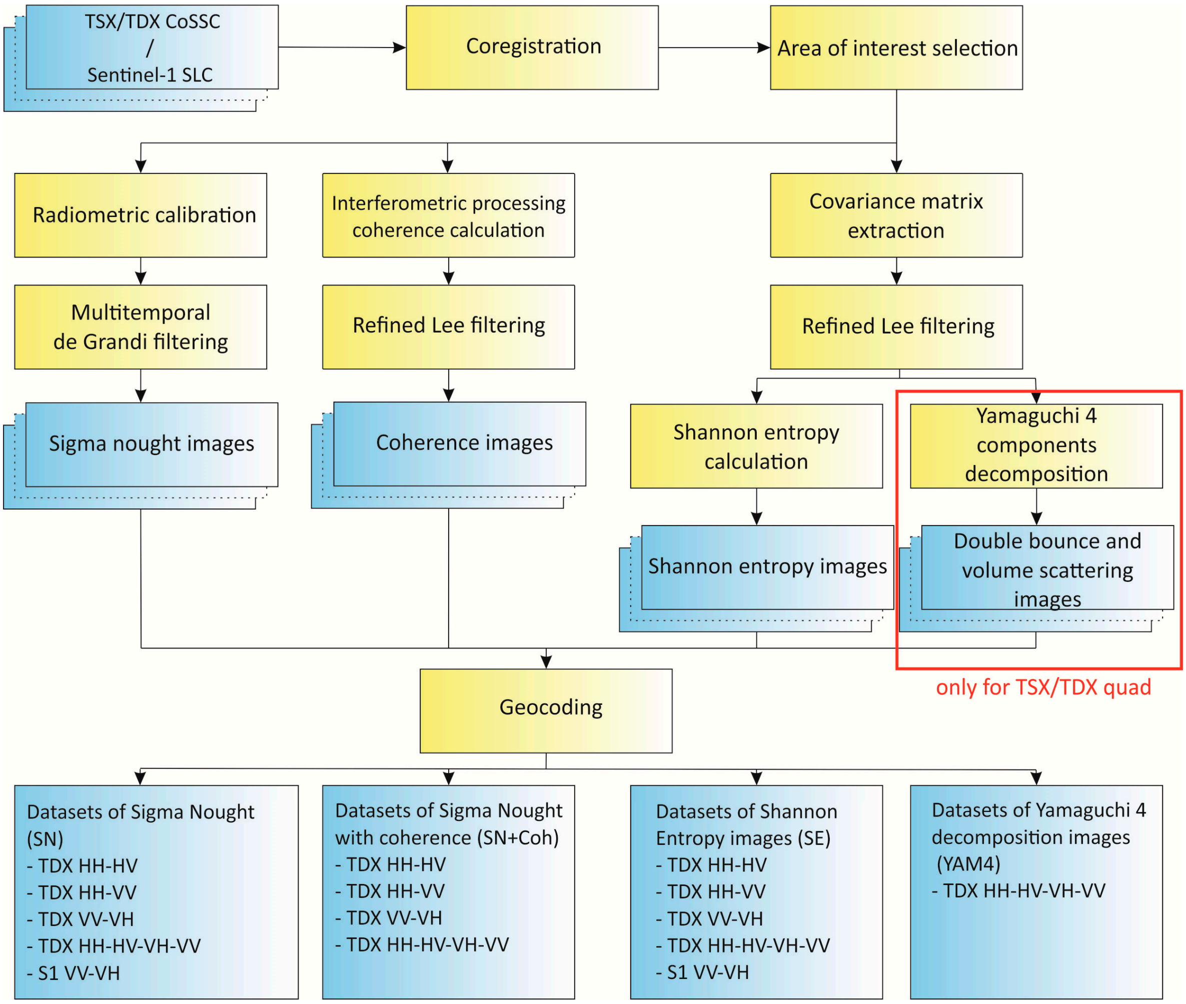

Figure 3. Workflow of images pre-processing.

The first step is image co-registration, which is followed by AoI selection. For both sensors, the radiometric calibration is performed using equations (1) and (2) [11,12]:

$$\beta^0_{LIN} = k_s(I^2 + Q^2) \tag{1}$$

where β^0_{LIN} is the radar brightness, called Beta Nought, k_s is the calibration coefficient, and I, Q are the real and imaginary parts of the backscattered complex signal, respectively. The β^0_{LIN} images are then converted into Sigma Nought images in logarithmic scale [dB]:

$$\sigma^0_{dB} = 10\, log_{10}(\beta^0_{LIN} \sin\theta) \tag{2}$$

where θ is the radar incidence angle. Prior to the conversion from linear to decibel scale, the multi-temporal de Grandi filter [13] is applied, using a 3 by 3 window, to reduce speckle effect, independently for each polarization channel for both image stacks. The calibrated and filtered images are then geocoded using a DEM from the SRTM mission [14,15], forming the First Dataset "Sigma Nought" (SN). Examples of colour compositions consisting of selected SN images are shown in Figures 4 and 5. The difference in resolution is clearly visible between TSX/TDX and S1A, as well as the contrast between land cover at HH and VV polarizations.

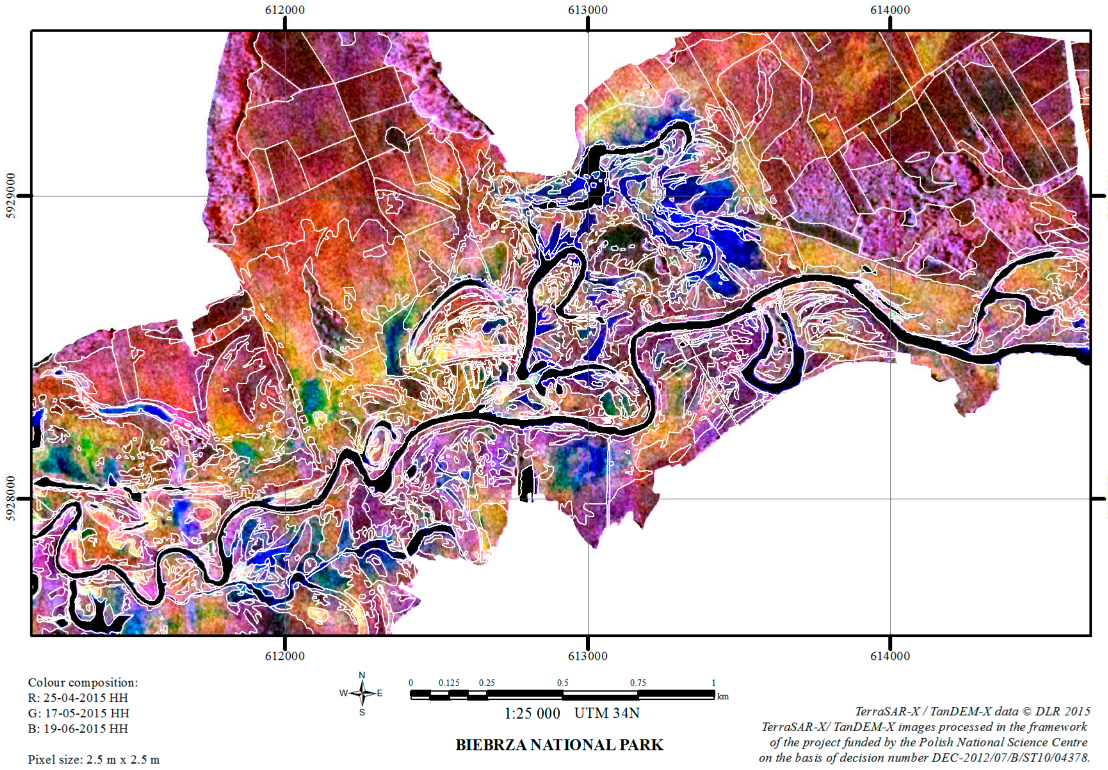

Figure 4. RGB colour composition of SN TSX images, with HH polarization, taken 25.04.2015, 17.05.2015 and 19.06.2015, respectively.

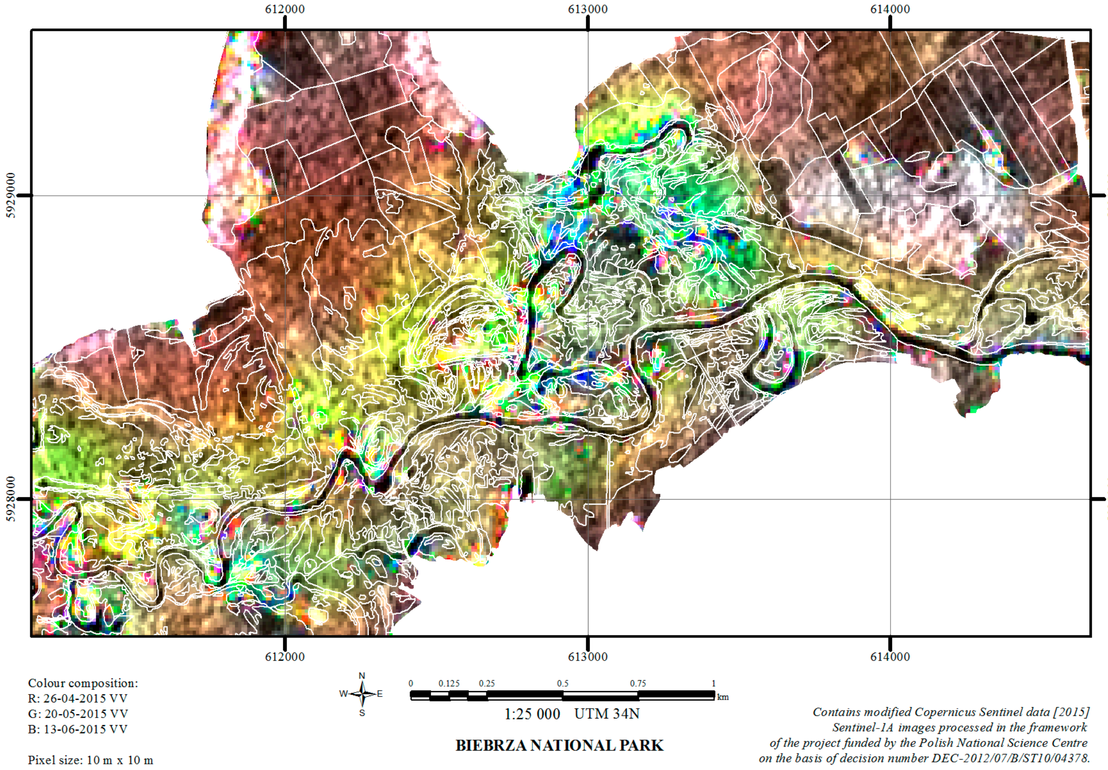

Figure 5. RGB colour composition of SN S1A images, with VV polarization, taken on 26.04.2015, 20.05.2015 and 13.06.2015, respectively.

Peer-reviewed version available at Remote Sens. 2018, 10, 78; doi:10.3390/rs10010078

The coherence is another parameter considered in this study. It is calculated between consecutive images, with temporal separation of 11 (TSX/TDX) and 12 days (S1A), using this formula [16]:

$$\gamma = \left| \frac{E[s_1 s_2^*]}{\sqrt{E[|s_1|^2]E[|s_2|^2]}} \right| \tag{3}$$

where γ is the coherence (ranging from 0 to 1), s_1 and s_2 are the complex SAR images, $E[\cdot]$ is the expected value, and $*$ indicates the complex conjugate.

Over the vegetated areas, the 11-day and 12-day coherence images showed very low values and no contrast, hence demonstrating to be not useful for mapping purposes. On the other hand, it was possible to compute the coherence of TSX/TDX data acquired quasi simultaneously in monostatic or bistatic tandem mode (with perpendicular baseline of 1.9 km and across baseline of 300 m). In such coherence images there are differences between different types of land cover, mostly between trees, open water and semi-natural herbaceous vegetation, e.g. see Figure 6. The contrast between land cover types depends on the date of acquisition and polarization. The contribution of this information was analysed in this study, considering a second dataset called "Sigma Nought + Coherence" (SN+coh). An example of colour composition using three coherence images corresponding to three different dates is shown in Figure 7. It can be observed that, for different parts of the image, the coherence is changing over time.

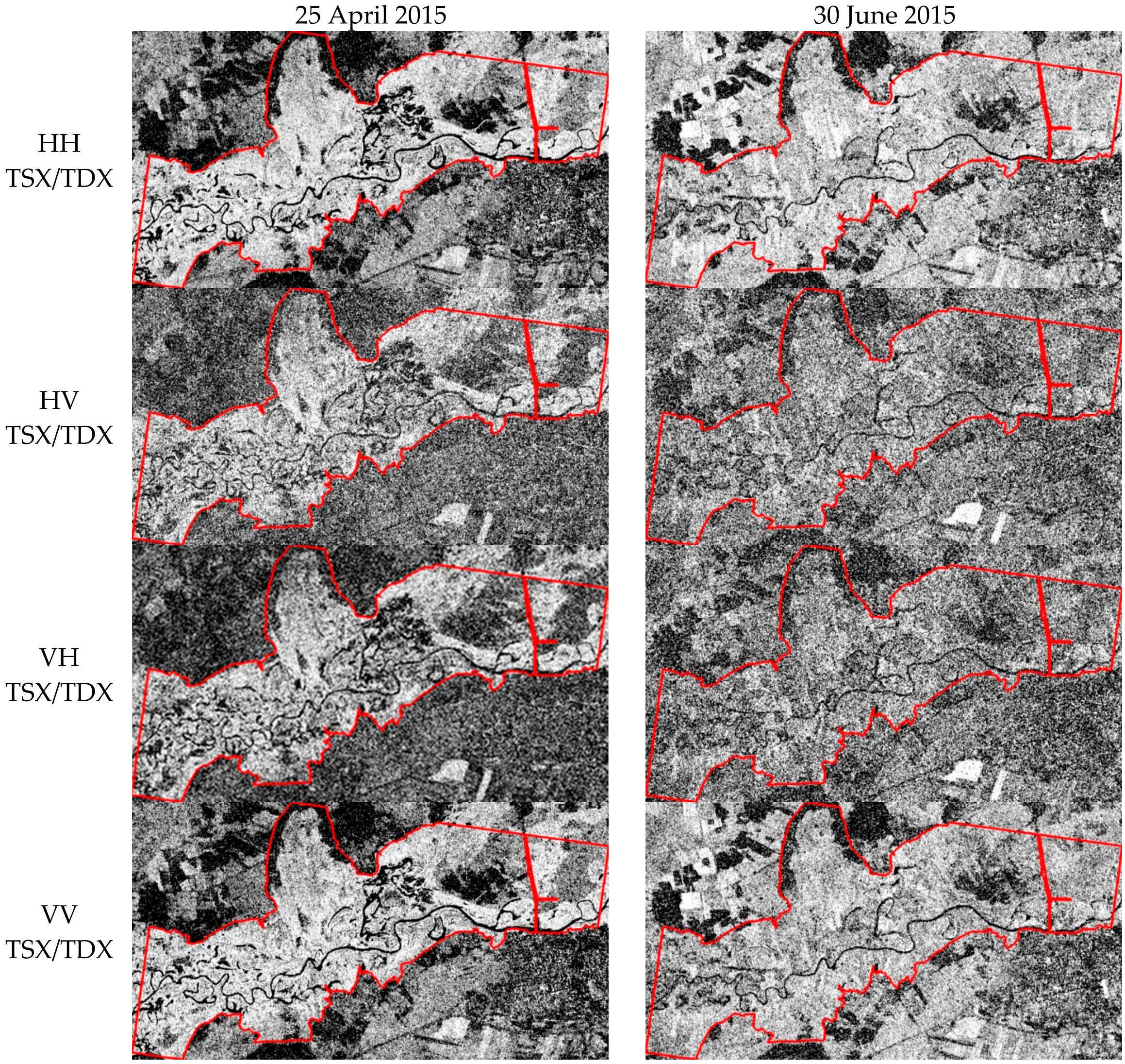

Figure 6. Examples of TSX/TDX coherence images for two different acquisition dates and four polarizations.

doi:10.20944/preprints201711.0003.v1

Peer-reviewed version available at *Remote Sens.* **2018**, *10*, 78; doi:10.3390/rs10010078

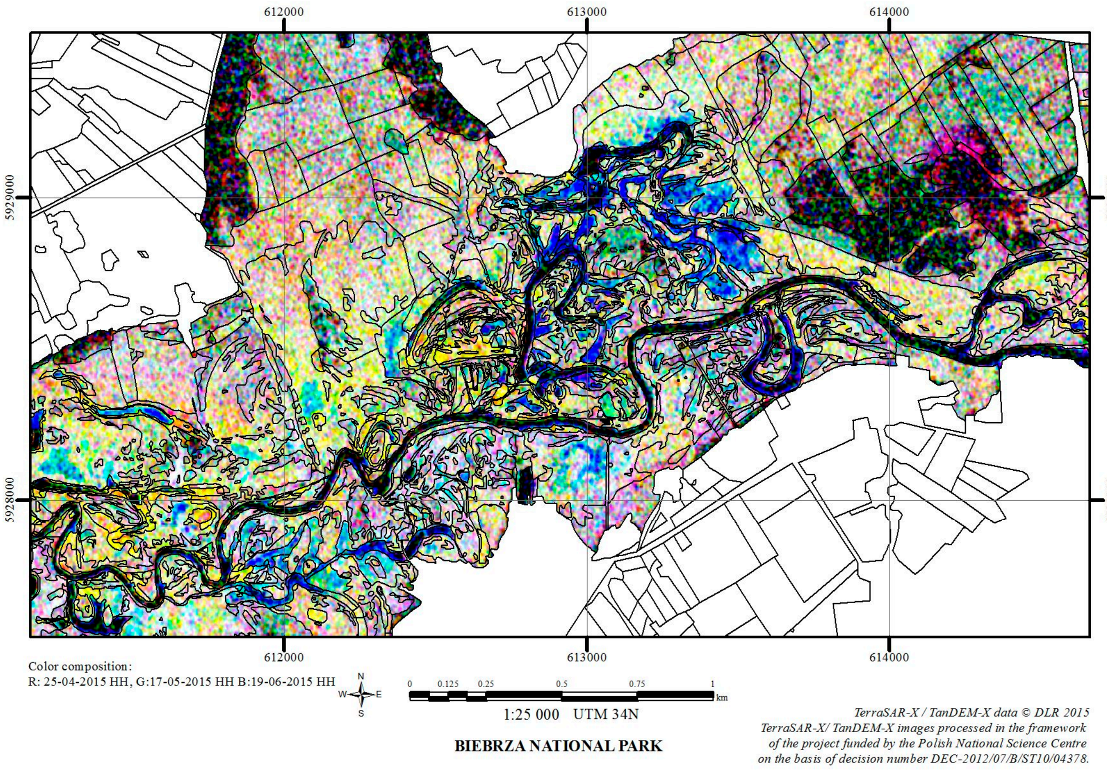

BIEBRZA NATIONAL PARK

TerraSAR-X / TanDEM-X data © DLR 2015
TerraSAR-X/ TanDEM-X images processed in the framework of the project funded by the Polish National Science Centre on the basis of decision number DEC-2012/07/B/ST10/04378.

Figure 7. RGB colour composition of the coherence change based on TSX/TDX images acquired at HH polarization, taken on 25.04.2015, 17.05.2015 and 19.06.2015, respectively.

The analysis of the polarimetric features of the considered data is another component of this study. This was done through polarimetric decompositions, which reveal the scattering mechanisms that are dependent on object structure, dimension and moisture and are classified in surface scattering, volume scattering and double bounce. The Shannon Entropy (SE) can be extracted from quad-pol (TSX/TDX) and dual-pol data (S-1 and TSX/TDX). SE, which measures the randomness of the scattering of a pixel [17], was extracted from a co-variance matrix using the PolSARpro software. SE is the sum of two contributions: intensity related (SE_I), which depends on total backscattered power, and polarimetry related (SE_P), which depends on the degree of polarization [18]. The SE is given by the following formulae [17,18]. For dual polarization data:

$$SE = \log \pi^2 e^2 \, |C_2| = SE_I + SE_P \tag{4}$$

$$SE_I = 2\log\left(\frac{\pi e I_c}{2}\right) = 2\log\left(\frac{\pi e Tr(C_2)}{2}\right) \tag{5}$$

$$SE_P = \log(1 - P_C^2) = \log\left(4\frac{|C_2|}{Tr(C_2)^2}\right) \tag{6}$$

For fully polarimetric data (quad-pol):

$$SE = \log \pi^3 e^3 \, |T_3| = SE_I + SE_P \tag{7}$$

$$SE_I = 3\log\left(\frac{\pi e I_T}{3}\right) = 3\log\left(\frac{\pi e Tr(T_3)}{3}\right) \tag{8}$$

$$SE_P = \log(1 - P_T^2) = \log\left(27\frac{|T_3|}{Tr(T_3)^3}\right) \tag{9}$$

where Tr is the trace of matrix, C_2 is the covariance matrix and T_3 is the coherence matrix, I_c, I_T is the intensity, P_c, P_T is the degree of polarization.

Preprints (www.preprints.org) | NOT PEER-REVIEWED | Posted: 1 November 2017 doi:10.20944/preprints201711.0003.v1

Peer-reviewed version available at Remote Sens. 2018, 10, 78; doi:10.3390/rs10010078

High values of the SE_P component, which means a high degree of phase randomness, were observed over open water and dense vegetation (grass). High values of SE_I and low values of SE_P are associated to the double bounce effect over urban areas and some crops, like corn outside of main AoI, as well as partially flooded vegetation and common reed in the AoI.

The polarimetric decomposition of TSX/TDX quad-pol data was based on the Yamaguchi 4-component decomposition, which has a direct physical interpretation. The general formula, which is described in details in [18,19], is:

$$\langle[C]\rangle = f_s\langle[C]\rangle_s + f_d\langle[C]\rangle_d + f_v\langle[C]\rangle_v + f_c\langle[C]\rangle_c \tag{10}$$

where $[C]$ is the co-variance matrix, f_s, f_d, f_v, f_c are coefficients, $\langle[C]\rangle_{s,d,v,c}$ are the mean co-variance matrices for each scattering mechanism: s – surface, d – double bounce, v – volume, c - helix.

The CoSSC TSX/TDX and the SLC S1A images were processed using PolSARPro 5.0 [20] and SARScape 5.0 [21,22]. Co-registration, radiometric calibration, test area selection, multi-temporal de Grandi filtering and interferometric processing, including coherence calculation and geocoding, were done using SARScape. The Lee speckle filtering [23], SE and the Yamaguchi 4-components decomposition were performed using PolSARPro. The output from the pre-processing stage are four datasets, which are listed in Table 3.

Table 3. Datasets for classification.

Dataset	Contents
SN	Sigma Nought images
SN + Coh	Sigma Nought and coherence images
SE	Shannon Entropy images
YAM4	Yamaguchi 4-component decomposition results (quad-pol data only)

2.4 Multitemporal image classification

"Per pixel" classification of the datasets shown in Table 3 was carried out to retrieve thematic classes. The classification workflow is shown in Figure 8. The first step was defining good and representative samples for the thematic classes (ROIs, Regions Of Interest) and calculating their statistical signatures: mean, variance and co-variances. The ROIs were identified using the ground truth data. The list of classes, the number of representing pixels and their surface are shown in Table 1. The quality of the samples (signatures) is expressed by the number of pixels, their surface and the mutual "spectral" separability. In fact, the supervised classification approach assumes that the thematic classes are sufficiently different spectrally. For each pair of classes, the separability was calculated using the Jeffries-Matussita Distance [24]. Other separability measures, like the Transformed Divergence, the Bhattacharyya distance [25,26] or the Hellinger distance [27] could also be applied.

If the separability verification is positive, the ROIs can then be split into training and control parcels and submitted to classification. Otherwise, the ROIs have to be merged following their spectral similarity and thematic significance. This can be a time-consuming process. In order to facilitate it, in this work a hybrid approach was adopted, which combines a supervised classification with an unsupervised clustering technique. The clusters automatically generated by the ISODATA algorithm [28], after their thematic aggregation based on ground truth, reveal the objects that are truly consistent in the spectral space. The unsupervised classification results make the ROIs redefinition faster and more appropriate for the further supervised classification. The steering parameters of clustering were carefully chosen because of the data heterogeneity. The following parameters were identified: minimum number of classes: 8; maximum number of classes: 12;

Peer-reviewed version available at *Remote Sens.* **2018**, *10*, 78; doi:10.3390/rs10010078

maximum iterations: 30; change threshold: 1%; minimum number of pixels in class: 100; maximum standard deviation: 1; minimum class distance: 3; and maximum merge pairs: 2.

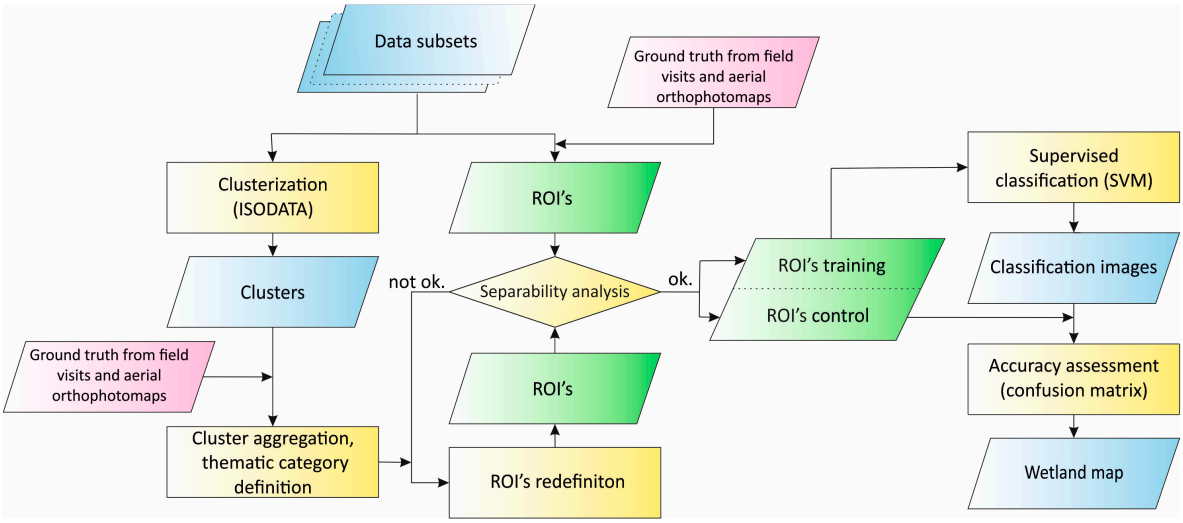

Figure 8. Workflow of thematic processing of the data subsets.

The supervised classification was performed using the Supported Vector Machine technique [17,29-31]. The advantage of this technique is that it does not require a large number of training samples [32], and the probability distribution is not assumed a priori [33]. The data were classified using radial basis function kernel, penalty parameter = 100 and a high classification probability threshold = 0.9. The quality of classification was analysed based on the classification accuracy, estimated by the Overall Accuracy (OAA) and the Kappa Index of Agreement (KIA) [34].

3. Results and discussion

In order to correctly interpret the achieved results, we remind the main goals of this work: i) mapping the vegetation types/associations/species and the temporarily or permanently flooded areas, and ii) comparing the performance of S1A and TSX/TDX for mapping purposes. The first goal embraces two interrelated phenomena: vegetation and water regime. In wetlands, the types of vegetation (species and associations) develop and grow as a consequence of a multiannual water regime. The vegetation is then an indicator of preponderant moisture conditions, and the temporarily or permanently flooded areas allow the development of diversified hygrophilous associations. Considering these aspects while performing wetland classification provides useful information for eco-hydrological investigations and for wetland management.

Referring to Table 1, some vegetation types (common reed, reed canary, sweet grass) have quite similar features regarding the microwave scattering mechanisms, e.g. broad leaves and thin stems. For this reason, the set of thematic classes from Table 1 turned out to be too detailed to be distinguished by classification of the multi-temporal SAR images collected in this experiment. In fact, the classification based on initial samples only achieved a low accuracy level (OAA<40%). It was then necessary to reduce the number of classes. For both the S1A and TSX/TDX datasets and an OAA exceeding of 40%, it was possible to distinguish 6 thematic categories: 1. permanent water bodies, 2. temporarily flooded areas, 3. wet grasslands, 4. dry grasslands, 5. common reed and 6. deciduous forest. The number of classes, which is sensibly smaller than expected at the beginning of the experiment, was fixed for all datasets submitted to classification. The results of the accuracy estimations are presented in Figure 9. It is worth mentioning that some researchers exclude a priori, from the list of land cover and vegetation types, the deciduous forest class, e.g. see [9]. This is done by supposing that their location is known and the backscattering features could worsen the overall classification accuracy. However, when the vegetation succession has to be analysed over years, like in this work, it is interesting to check the possibility of identifying this class within the other wetland vegetation classes.

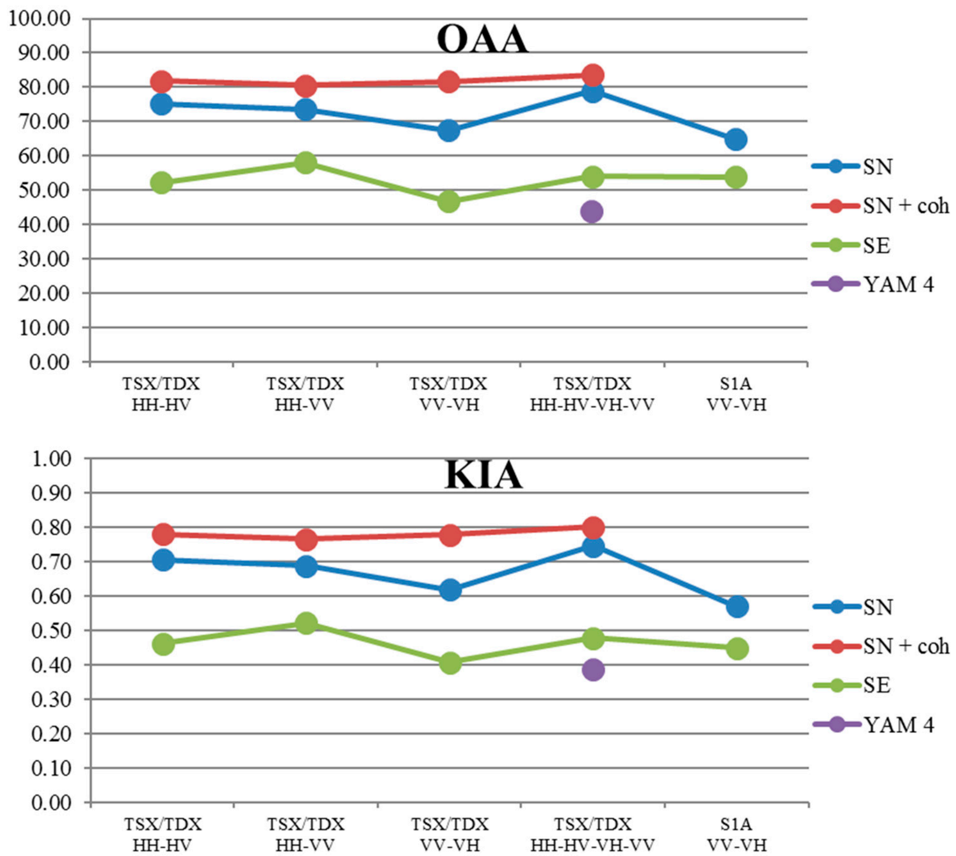

Figure 9. Results of the accuracy assessment for the S1A and TSX/TDX datasets: a) overall accuracy - OAA, b) Kappa Index of Agreement – KIA

The results can be summarized as follows, relating them to the aspects addressed in the introduction:

1. Mapping wetland with C-band S1A alone, based on multi-temporal series of SAR images with the VV/VH polarization. The results achieved with time series of S1A SN are quite poor: the OAA for all classes equals 65% and KIA is 0.58. These values are not satisfactory. For this reason, the S1A dataset is not recommended for herbaceous wetland mapping in the Biebrza valley. There is a second disadvantageous feature of the S1A dataset: its geometric resolution is too coarse to detect small areas of vegetation associations adjacent to oxbows and floodplain lakes.
2. Mapping wetland with the experimental fully polarimetric quad-pol X-band TSX/TDX data. The results achieved with this dataset (polarizations VV/VH/HV/HH) are the best amongst all SN time series. The OAA is 79 %, with a high coefficient of agreement KIA of 0.75. The results achieved using the fully polarimetric data and the Yamaguchi 4-component decomposition (YAM4) are less useful than expected: the OAA is 43% and KIA is 0.39. For this area and for the majority of classes over time, the dominant scattering mechanism is volume scattering, which decreases the OAA. The advantage of this decomposition is revealing partially flooded herbaceous vegetation by double bounce effect for particular TSX/TDX acquisitions. The results achieved using SE decomposition are better than for the YAM4 dataset: the OAA is 55% and KIA is 0.48. This can be caused by intensity component contribution besides of polarimetric behaviour.
3. Compare wetland mapping using the dual polarization TSX/TDX subsets, i.e. HH-HV, HH-VV and VV-VH. For the dual-pol TSX/TDX products, the OAA and KIA are smaller than the ones of the four polarizations dataset: OAA=76% and KIA=0.71 for HH/HV; OAA=74% and KIA=0.69 for HH/VV; and OAA=68% and KIA=0.63 for VV/VH. However, there is a relatively small

difference between the results achieved by quad-pol and the best dual-pol (HH/HV): this configuration can be recommended for wetland mapping purposes.

4. Compare wetland mapping using S1A and TSX/TDX, considering the same polarization (VV-VH) and covering the same observation period. The TSX/TDX datasets shoved the best performance. The difference of the OAA for the S1A and TSX/TDX datasets is about 3%. It seems that the coarser geometric resolution has a negative influence on the results achieved by the S1A dataset.
5. Study the suitability of the Shannon Entropy as polarimetric descriptor of wetland land cover. The results achieved with the SE time series are quite poor, with the OAA ranging from 47% to 58%, and KIAs ranging between 0.41 and 0.52. As a consequence, this dataset is not recommended for mapping of the herbaceous wetland at hand. The OAA values are lower for the pairs of bands containing cross-pol components (VH or HV). According to [17], these components are strongly affected by the noise equivalent sigma zero over wetlands areas: this affects the SE parameter.
6. Assess the contribution of the interferometric coherence as an additional layer for land cover classification. The interferometric coherence estimated for the acquisitions of S1A, with 12-day interval, and TSX/TDX, with 11-day interval, turned out to be useless as land cover discriminator over this wetland. On the other hand, the coherence calculated for the TSX/TDX interferometric pairs acquired simultaneously causes an increase of the OAA comparing to the SN time series. The OAA increases 7% for the HH-HV and HH-VV, 15% for the VV-VH, and only 4% for the VV-VH-HV-HH dataset. The interferometric coherence is considered here as an important asset of quad-pol TSX/TDX acquisitions.

Figure 10 shows a classification result over the AoI obtained using SN and coherence time series of TSX/TDX data (four polarizations). This configuration achieved the best classification accuracy (OAA = 83%, KIA=0.80).

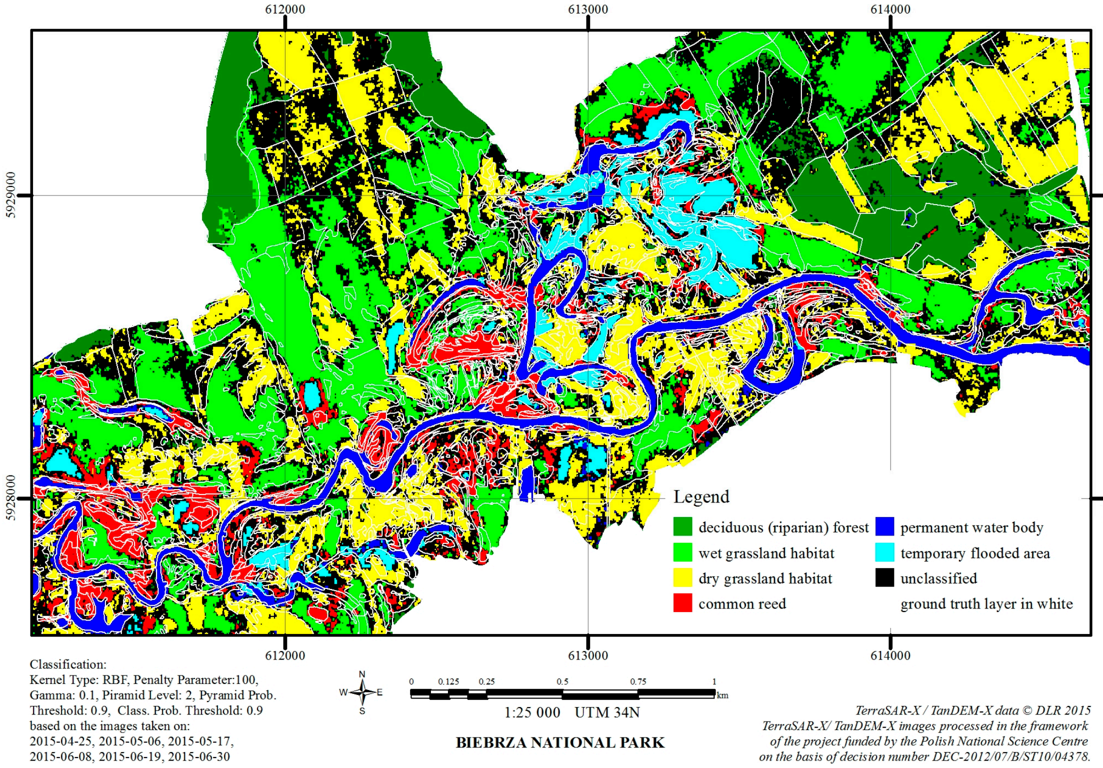

Classification:
Kernel Type: RBF, Penalty Parameter:100,
Gamma: 0.1, Piramid Level: 2, Pyramid Prob.
Threshold: 0.9, Class. Prob. Threshold: 0.9
based on the images taken on:
2015-04-25, 2015-05-06, 2015-05-17,
2015-06-08, 2015-06-19, 2015-06-30

TerraSAR-X / TanDEM-X data © DLR 2015
TerraSAR-X/ TanDEM-X images processed in the framework
of the project funded by the Polish National Science Centre
on the basis of decision number DEC-2012/07/B/ST10/04378.

Figure 10. Classification map of the AoI obtained using sigma nought and coherence time series of TSX/TDX data (four polarizations). This configuration achieved the best classification accuracy (OAA = 83%, KIA=0.80).

4. Conclusions

In this comparative study, the use of S1A and TSX/TDX image time series for herbaceous wetland mapping has been evaluated. The main components of the methodology used to carry out this work have been presented. Different aspects of data processing and analysis have been described. The main outcomes of the study are briefly summarized below.

Using image classification, in the AoI only the main land cover types could be distinguished. In fact, exceeding an OAA of 40% for both the S1A and TSX/TDX datasets, it was possible to distinguish six thematic categories: 1. permanent water bodies, 2. temporarily flooded areas, 3. wet grasslands, 4. dry grasslands, 5. common reed and 6. deciduous forest. In terms of vegetation mapping, the majority of species identified in situ (listed in Table 1) had to be merged into two main categories: wet grassland habitat and dry grassland habitat. Concerning water stagnation mapping, it was possible to classify permanent water bodies and temporarily flooded areas. This second category includes the partially flooded grasslands that could be identified and mapped through the Shannon Entropy decomposition exploiting the double bounce effect.

At the beginning of the project, the S1A imagery was identified as a primary dataset for thematic mapping. However, the S1A results achieved in this study show an important limitation of this type of data for the purpose of a detailed wetland mapping. Advantages of S1A include its large area coverage and the possibility to extract information on partially flooded grasslands for the whole Biebrza valley area using the SE.

The results achieved using time series of TSX/TDX images, especially those taken in fully polarimetric mode, show that the wetland mapping of above mentioned classes can be performed with satisfying accuracy, better than the one achieved using S1A. The use of the four polarisations dataset shows the best accuracy using sigma nought values only. In addition, the use of the interferometric coherence, extracted from TSX/TDX images acquired simultaneously, slightly increases this accuracy (2.5%).

The comparison of the results from the different dual polarisations (HH-HV, HH-VV and VV-VH) versus the four polarisations leads to the conclusion that standard TSX/TDX product, acquired at HH-HV polarisation, provides the best data for wetland mapping. Similarly to S1A, also in this case the partially flooded vegetation can be properly extracted using SE: in this case there is the additional advantage of a higher geometric resolution with respect to the S1A dataset. The TSX/TDX results achieved in this work lead to the conclusion that TSX/TDX sensors are well-suited to the needs of this wetland mapping in terms of water time stagnation and its ecological implications, especially for fine oxbows and small floodplain lakes.

Acknowledgments: This publication was prepared in the frame of the MARSHALL project, funded by the Polish National Science Centre (DEC-2012/07/B/ST10/04378). The authors acknowledge the German Space Agency DLR for providing the TerraSAR-X / TanDEM-X Quad-Pol images in the frame of the NTI_POLI 6756 “Oxbow Plus” project. This work contains modified Copernicus Sentinel data.

Conflicts of Interest: The authors declare no conflict of interest.

References

1. Brisco, B. Mapping and monitoring surface water and wetlands with synthetic aperture radar. In *Remote Sensing of Wetlands Applications and Advances* R.W. Tiner, M.W. Lang, V.V. Klemas, CRC Press 2015; pp 119-136.
2. Dabrowska-Zielinska, K.; Budzynska, M.; Tomaszewska, M.; Bartold, M.; Gatkowska, M.; Malek, I.; Turlej, K.; Napiorkowska, M. Monitoring wetlands ecosystems using ALOS PALSAR (L-band, HV) supplemented by optical data: A case study of Biebrza wetlands in Northeast Poland. *Remote Sensing* **2014**, *6*, 1605-1633.
3. Dabrowska-Zielinska, K.; Budzynska, M.; Tomaszewska, M.; Bartold, M.; Gatkowska, M. The study of multifrequency microwave satellite images for vegetation biomass and humidity of the

Peer-reviewed version available at *Remote Sens.* **2018**, *10*, 78; doi:10.3390/rs10010078

area under Ramsar convention. *2015 IEEE International Geoscience and Remote Sensing Symposium (IGARSS)* **2015**, 5198-5200.

4. Hong, S.H.; Wdowinski, S. Double-bounce component in cross-polarimetric sar from a new scattering target decomposition. *Ieee Transactions on Geoscience and Remote Sensing* **2014**, *52*, 3039-3051.
5. Kim, S.W.; Wdowinski, S.; Amelung, F.; Dixon, T.H.; Won, J.S. Interferometric coherence analysis of the everglades wetlands, South Florida. *Ieee Transactions on Geoscience and Remote Sensing* **2013**, *51*, 5210-5224.
6. Touzi, R. Target scattering decomposition in terms of roll-invariant target parameters. *Ieee Transactions on Geoscience and Remote Sensing* **2007**, *45*, 73-84.
7. Baghdadi, N.; Bernier, M.; Gauthier, R.; Neeson, I. Evaluation of c-band sar data for wetlands mapping. *International Journal of Remote Sensing* **2001**, *22*, 71-88.
8. Biebrza national park. https://www.biebrza.org.pl/lang,2 (accessed 31.10.2017).
9. Ramsar list. http://www.ramsar.org/sites/default/files/documents/library/sitelist.pdf (accessed 29.10.2017).
10. Hajnsek, I.; Busche, T.; Krieger, G.; Zink, M.; Schulze, D.; Moreira, A. *Tandem-X ground segment, announcement of opportunity: Tandem-X Science Phase*. 2014; p 27.
11. Nuno, M.; Meadows, P.J. Radiometric calibration of s-1 level-1 products generated by the Sentinel-1 IPF https://sentinel.esa.int/documents/247904/685163/S1-Radiometric-Calibration-V1.0.pdf (accessed 15.10.2017),
12. Radiometric calibration of terrasar-x data, beta naught and sigma naught coefficient calculation. http://www.intelligence-airbusds.com/files/pmedia/public/r465_9_tsx-x-itd-tn-0049-radiometric_calculations_i3.00.pdf (accessed 25.09.2017),
13. Grandi, G.F.D.; Leysen, M.; Lee, J.S.; Schuler, D. Radar reflectivity estimation using multiple sar scenes of the same target: Technique and applications. *1997 IEEE International Geoscience and Remote Sensing Symposium (IGARSS)*, **1997**, pp 1047-1050 vol.1042.
14. Rosen, P.A.; Hensley, S.; Gurrola, E.; Rogez, F.; Chan, S.; Martin, J.; Rodriguez, E. SRTM C-band topographic data: Quality assessments and calibration activities. 2001 *IEEE International Geoscience and Remote Sensing Symposium (IGARSS)* **2001**, 739-741.
15. Rosen, P.; Eineder, M.; Rabus, B.; Gurrola, E.; Hensley, S.; Knopfle, W.; Breit, H.; Roth, A.; Werner, M. Srtm-mission - cross comparison of x and c band data properties. 2001 *IEEE International Geoscience and Remote Sensing Symposium (IGARSS)* **2001**, 751-753.
16. Hanssen, R.F. *Radar interferometry : Data interpretation and error analysis*. Kluwer Academic: Dordrecht ; Boston, 2001; p xviii, 308 p.
17. Betbeder, J.; Rapinel, S.; Corgne, S.; Pottier, E.; Hubert-Moy, L. Terrasar-X dual-pol time-series for mapping of wetland vegetation. *ISPRS Journal of Photogrammetry and Remote Sensing* **2015**, *107*, 90-98.
18. Lee, J.-S.; Pottier, E. Polarimetric radar imaging : From basics to applications. In *Optical science and engineering 143*, Taylor and Francis,: Boca Raton, 2009; pp 1 online resource (xxiv, 398 pages).
19. Cloude, S.; Oxford University Press. Polarisation applications in remote sensing. Oxford University Press,: Oxford, 2010; online resource, 453 p.

20. Pottier, E.; Ferro-Famil, L. Polsarpro v5.0: An esa educational toolbox used for self-education in the field of polsar and pol-insar data analysis. *2012 Ieee International Geoscience and Remote Sensing Symposium (IGARSS)* **2012**, 7377-7380.
21. Sarmap sa. http://www.sarmap.ch/index.php (accessed 31.10.2017)
22. Simonetto, E.; Follin, J.-M. An overview on interferometric sar software and a comparison between doris and sarscape packages. In *Geospatial free and open source software in the 21st century: Proceedings of the first open source geospatial research symposium, OGRS 2009*, Bocher, E.; Neteler, M., Eds. Springer Berlin Heidelberg: Berlin, Heidelberg, 2012; pp 107-122.
23. Lee, J.S. Speckle analysis and smoothing of synthetic aperture radar images. *Computer Graphics and Image Processing* **1981**, *17*, 24-32.
24. Richards, J.A. *Remote sensing with imaging radar*. Springer Berlin Heidelberg: 2009.
25. Morio, J.; Refregier, P.; Goudail, F.; Dubois-Fernandez, P.; Dupuis, X. A characterization of shannon entropy and Bhattacharyya measure of contrast in polarimetric and interferometric sar image. *Proceedings of the Ieee* **2009**, *97*, 1097-1108.
26. Chung, J.; Kannappan, P.; Ng, C.; Sahoo, P. Measures of distance between probability-distributions. *Journal of Mathematical Analysis and Applications* **1989**, *138*, 280-292.
27. Lee, K.Y.; Bretschneider, T.R. Separability measures of target classes for polarimetric synthetic aperture radar imagery. *Asian Journal of Geoinformatics* **2012**, *12*.
28. J.T. Tou,.; R.C, Gonzalez. *Pattern recognition principles*. 1st ed.; Addison-Wesley Publishing Company 1974.
29. Lardeux, C.; Frison, P.L.; Rudant, J.P.; Souyris, J.C.; Tison, C.; Stoll, B. In *Use of the SVM classification with polarimetric sar data for land use cartography*, 2006 IEEE International Symposium on Geoscience and Remote Sensing. **2006**, pp 493-496.
30. Shah Hosseini, R.; Entezari, I.; Homayouni, S.; Motagh, M.; Mansouri, B. Classification of polarimetric SAR images using support vector machines. *Canadian Journal of Remote Sensing* **2011**, *37*, 220-233.
31. Sukawattanavijit, C.; Chen, J.; Zhang, H. *GA-SVM algorithm for improving land-cover classification using SAR and optical remote sensing data*. 2017; Vol. PP, p 1-5.
32. Mantero, P.; Moser, G.; Serpico, S.B. In *Partially supervised classification of remote sensing images using SVM-based probability density estimation*, IEEE Workshop on Advances in Techniques for Analysis of Remotely Sensed Data, 2003, 27-28 Oct. 2003, 2003; pp 327-336.
33. Özdogan, M. Image classification methods in land cover and land use. In *Remotely sensed data characterization, classification, and accuracies*, P.S. Thenkabail; CRC Press: 2015; pp 231-246.
34. Hudson W.D., Ramm C.W. Correct formulation of the Kappa Coefficient of Agreement. In *Remote Sensing Thematic Accuracy Assessment: A Compendium.* Fenstermaker L.K. American Society for Photogrammetry and Remote Sensing, 1994; pp. 266-267.